

Debris-Covered Glacier Energy Balance Model for Imja-Lhotse Shar Glacier in the Everest Region of Nepal

D. R. Rounce¹, D. J. Quincey², and D. C. McKinney¹

[1]{Center for Research in Water Resources, University of Texas at Austin, Austin, Texas, USA}

[2]{School of Geography, University of Leeds, Leeds, LS2 9JT, UK}

Correspondence to: D. R. Rounce (david.rounce@utexas.edu)

Keywords: Debris-covered glaciers, Himalaya, Energy Balance, Structure from Motion, Ablation, Surface Roughness

Abstract

Debris thickness plays an important role in regulating ablation rates on debris-covered glaciers as well as controlling the likely size and location of supraglacial lakes. Despite its importance, lack of knowledge about debris properties and associated energy fluxes prevents the robust inclusion of the effects of a debris layer into most glacier surface energy balance models. This study combines fieldwork with a debris-covered glacier energy balance model to estimate debris temperatures and ablation rates on Imja-Lhotse Shar glacier located in the Everest region of Nepal. The debris properties that significantly influence the energy balance model are the thermal conductivity, albedo, and surface roughness. Fieldwork was conducted to measure thermal conductivity and a method was developed using Structure from Motion to estimate surface roughness. Debris temperatures measured during the 2014 melt season were used to calibrate and validate a debris-covered glacier energy balance model by optimizing the albedo, thermal conductivity, and surface roughness at 10 debris-covered sites. Furthermore, three methods for estimating the latent heat flux were investigated. Model calibration and validation found the three methods had similar performance; however, comparison of modeled and measured ablation rates revealed that assuming the latent heat flux is zero may overestimate ablation. Results also suggest that where debris moisture is unknown, measurements of the relative humidity or precipitation may be used to estimate wet debris periods, i.e., when the latent heat flux is non-zero. The effect of temporal resolution on the model was also assessed and results showed that both 6-hour data and daily average data slightly underestimate debris

1 temperatures and ablation rates, thus these should only be used to estimate rough ablation rates
2 when no other data are available.

3

4 **1 Introduction**

5 Debris-covered glaciers are commonly found in the Everest region of Nepal and have important
6 implications with regard to glacier melt and the development of glacial lakes. It is well
7 understood that a thick layer of debris (i.e. > several cm) insulates the underlying ice, while a
8 thin layer of debris (i.e. < several cm) may enhance ablation (Østrem, 1959; Nakawo and Young,
9 1981; Nicholson and Benn, 2006; Reid et al., 2012). Spatial variations in debris thickness,
10 particularly where the debris layer thins up-glacier, can also lead to reverse topographic and
11 ablation gradients, glacier stagnation and, ultimately, the development of lakes (Benn et al.,
12 2012). These glacial lakes and their surrounding bare ice faces also play a crucial role in glacier
13 melt as they typically have ablation rates that are orders of magnitude greater than those
14 observed beneath debris cover (Benn et al., 2012). The importance of debris thickness has led
15 many studies to develop models in conjunction with knowledge of the surface temperature to
16 derive debris thickness (Zhang et al., 2011; Foster et al., 2012; Fujita and Sakai, 2014; Rounce
17 and McKinney, 2014). With knowledge of debris thickness, energy balance models may be used
18 to model debris surface temperature, sub-debris ablation rate, and/or runoff downstream
19 (Nicholson and Benn, 2006; Reid et al., 2012; Collier et al., 2014; Fujita and Sakai, 2014). The
20 main factors affecting the performance of these models are the amount of knowledge of the
21 debris properties, the spatial and temporal resolution of the meteorological data, and the
22 assumptions/complexity of the model.

23 The properties of the debris typically required in debris-covered glacier energy balance models
24 are the albedo, thermal conductivity, and surface roughness. The albedo of debris on glaciers in
25 the Everest region has been found to range from 0.1 – 0.6 (Inoue and Yoshida, 1980; Kayastha et
26 al., 2000; Nicholson and Benn, 2012; LeJeune et al., 2013). Specifically, Nicholson and Benn
27 (2012) reported that 62% of measured values ranged between 0.1 and 0.3. Similarly, Kayastha et
28 al. (2000) showed that most values fall between 0.2 and 0.4. The thermal conductivity of debris
29 in the Everest region has been found to range from 0.60 to 1.29 W m⁻¹ K⁻¹ (Conway and
30 Rasmussen, 2000; Nicholson and Benn, 2012; Rounce and McKinney, 2014). The surface

1 roughness, z_0 , is arguably the most difficult parameter to measure as it requires an eddy
2 covariance instrument, horizontal wind speed measurements at multiple heights above the
3 surface, or detailed microtopographic measurements (Brock et al., 2006). In the Everest region,
4 Inoue and Yoshida (1980) estimated z_0 to be 0.0035 m and 0.060 m for two sites, one consisting
5 of small schist and bare ice and another comprising mainly large granite, respectively. Takeuchi
6 et al. (2000) estimated a similar value of z_0 on the Khumbu glacier of 0.0063 m. On Miage
7 glacier in the Italian Alps, Brock et al. (2010) measured z_0 to be 0.016 m on a debris-covered
8 glacier.

9 In addition to the properties of the debris, the amount and source of meteorological data available
10 may also greatly influence the model performance. In particular, knowledge related to the latent
11 heat flux on debris-covered glaciers is very limited. This has led previous studies to assume the
12 surface is dry (Foster et al., 2012; Lejeune et al., 2013; Rounce and McKinney, 2014), assume it
13 is dry unless the surface relative humidity was 100% (Reid and Brock 2010; Reid et al., 2012;
14 Fyffe et al., 2014), assume a relationship between debris thickness and wetness (Fujita and Sakai,
15 2014), or use a reservoir approach to model the moisture in the debris (Collier et al., 2014).
16 Collier et al. (2014) suggested that if the atmospheric surface layer is well mixed, then the water
17 vapor partial pressure between the surface and the air may be assumed to be constant, thereby
18 resulting in a latent heat flux based on the vapor pressure gradient. Fyffe et al. (2014) also
19 commented that the lower portion of the debris near the ice interface was observed to be
20 saturated indicating that there may be evaporation and condensation occurring within the debris,
21 albeit small, even when the surface relative humidity is less than 100%. The lack of knowledge
22 of the moisture in the debris and at its surface makes it difficult to accurately model the latent
23 heat flux term. These problems are further exacerbated in data scarce regions where automatic
24 weather stations are not available. In these situations, reanalysis datasets must be used for all the
25 required meteorological data (Fujita and Sakai, 2014).

26 This study develops a method to estimate z_0 using a microtopographic method in conjunction
27 with Structure from Motion (SfM) photogrammetry techniques (Westoby et al., 2012). The z_0
28 values are used with measured values of thermal conductivity, and previously reported values of
29 albedo to calibrate a debris-covered glacier energy balance model on Imja-Lhotse Shar glacier.
30 Temperature sensors installed at various depths at debris-covered sites were operated from May
31 to November 2014 on Imja-Lhotse Shar glacier and are used for calibration and validation of the

1 model. Various methods for estimating the latent heat flux are investigated. Furthermore, sub-
2 debris ablation rates are compared to ablation stake measurements to assess model performance
3 and the effects of temporal resolution are investigated.

4 5 **2 Data**

6 **2.1 Field Data**

7 Field research was conducted on the debris-covered portion of Imja-Lhotse Shar glacier
8 (27.901°N, 86.938°E, ~5050 m a.s.l., Figure 1) from May to November 2014. Imja-Lhotse Shar
9 glacier refers to both Imja glacier and Lhotse Shar glacier, which are avalanche-fed debris-
10 covered glaciers that converge and terminate into Imja Lake. The debris primarily consists of
11 sandy boulder gravel (Hambrey et al., 2008) with the debris thickness increasing towards the
12 terminal moraine. A more detailed description of the glacier may be found in Rounce and
13 McKinney (2014). The field expedition focused on 19 sites on the debris-covered portion of the
14 glacier to determine how debris thickness and topography affect ablation rates. Four sites were
15 used to analyze the surface roughness through the use of SfM and are referred to as Sites A-D
16 (Figure 2). These sites were selected to represent various grain sizes and mixes of debris that
17 were observed on Imja-Lhotse Shar glacier. Site A was relatively homogenous with the majority
18 of debris being cobble and gravel ranging in size from 0.05 to 0.25 m. Site B comprised similar
19 cobbles typically ranging in size from 0.15 to 0.25 m with larger boulders lying on top of the
20 cobble of up to 1.0 m. Site C had the finest debris, which primarily consisted of fines and gravel
21 with some cobbles on the surface up to 0.15 m in size. Lastly, Site D was the most
22 heterogeneous site with boulders ranging up to 0.40 m overlying a surface of cobble of similar
23 size to Site A mixed with the fine and gravel material found in Site C.

24 Temperature sensors and ablation stakes were installed at 20 other sites; however, data could
25 only be retrieved from 15 of the sites (Table 1) as sensors were lost due to large changes in the
26 topography and some of the loggers failed. Sites 4-14 were located in a single area that appeared
27 to have developed from differential backwasting over the years. This was the same focus area as
28 described in Rounce and McKinney (2014) and was selected because it appeared to be
29 representative of the debris-covered terrain on Imja-Lhotse Shar glacier and was accessible.
30 Sites 15-20 were located outside of the focus area in an adjacent melt basin to determine if the

1 focus area was representative of other debris-covered areas. At each site, the debris thickness
2 was determined following the methods described in Rounce and McKinney (2014) with the
3 exception of Site 4, where the debris thickness was greater than 1.0 m and therefore was
4 estimated assuming a linear temperature profile from the mean temperatures over the study
5 period similar to the extrapolation used in Nicholson and Benn (2012). The debris thickness of
6 these sites ranged from 0.07 m to greater than 1.0 m. A debris thickness of 1.0 m was considered
7 the maximum due to labor constraints. The slope was also approximated by measuring two
8 points, one 0.5 m uphill from the site and the other 0.5 m downhill, using a total station (Sokkia
9 SET520, $\pm 2.6\text{mm}/100\text{m}$). The slope at each site ranged from 17° to 37° . The aspect of each site
10 was measured using a compass (Table 1).

11 Temperature sensors (TR-42 ThermoRecorder, T&D Corporation) were installed and
12 successfully retrieved at 10 sites. These sensors recorded data every half hour from 19 May to
13 09 November 2014. Each of the 10 sites had a sensor at its surface, which was considered to be
14 installed 1 cm into the debris since debris was placed on top of the sensor. Sites 4, 11, 13, and
15 14 also had temperature sensors installed within the debris to capture the nonlinear temperature
16 variations in the debris and at three of the four sites the sensors were retrieved such that the
17 thermal conductivity could be estimated (Conway and Rasmussen, 2000).

18 Ablation stakes were also installed at 14 sites. One site had a debris thickness greater than 1.0 m,
19 so an ablation stake could not be installed. The ablation stakes were installed by excavating to
20 the debris-ice interface, at which point the debris thickness was measured, and then a 2 inch
21 diameter hole was drilled vertically approximately 1.0 m into the ice using a manual ice drill
22 (Kovacs Enterprise). A 2.0 m piece of 1 ½ inch PVC pipe was placed into the hole and the
23 height from the top of the ice to the top of the pipe was measured to determine the exact length
24 that the PVC pipe was inserted into the ice. A PVC end cap was then placed on top of the pole to
25 prevent anything from entering the hole through the pipe. The debris was then replaced in its
26 approximate original position.

27 **2.2 Meteorological Data**

28 The meteorological data used in the model calibration and validation was from an automatic
29 weather station (AWS), Pyramid Station (27.959° N, 86.813° E, 5035 m a.s.l., SHARE Network
30 operated by EV-K²-CNR), located off-glacier, next to the Khumbu glacier, approximately 14 km

1 northwest of Imja-Lhotse Shar glacier. The meteorological data provided by Pyramid Station
2 were unvalidated, i.e., prior to their quality control processing, minute measurements of air
3 temperature, wind speed, relative humidity, global radiation, precipitation, and snow depth. The
4 data were processed to be consistent with the half-hour debris temperature measurements on
5 Imja-Lhotse Shar glacier. The air temperature, wind speed, relative humidity, and global
6 radiation data were reviewed and deemed plausible, so no adjustments were performed. The
7 half-hour precipitation data was determined by summing the precipitation over each half-hour
8 time step. A few of the minute measurements recorded negative precipitation, which were
9 assumed to be zero as negative precipitation is not feasible. The half-hour snow depth data was
10 processed to assume a snow depth of zero if snow was not recorded on the ground for the entire
11 half-hour. The average snow depth over the half-hour was then computed and any average snow
12 depth less than 0.001 m was considered to be zero. Wind speed data were collected at 5 m and
13 adjusted to 2 m to be consistent with air temperature measurements for the turbulent heat fluxes
14 assuming a logarithmic dependence (Fujita and Sakai, 2014). The snow depth data were used to
15 derive a snowfall rate assuming a density of snow of 150 kg m^{-3} . The data were available from
16 31 May to 12 October 2014 with a few short gaps (missing 11.9% data). The first two days of
17 meteorological data were used as start-up time for the model.

18 Longwave radiation was not measured at Pyramid Station during this period; therefore, the
19 downward longwave radiation flux from NCEP/NCAR reanalysis data (Kalnay et al., 1996) was
20 used with a minor modification. A comparison of the downward longwave radiation flux from
21 NCEP/NCAR and the incoming longwave radiation flux at Pyramid Station from 2003 to 2010
22 (neglecting any data gaps) between the months of June and September revealed that
23 NCEP/NCAR overestimated the incoming longwave radiation by an average of 29 W m^{-2}
24 (results not shown). Therefore, the NCEP/NCAR downward longwave radiation flux was
25 adjusted to account for this overestimation when being used in conjunction with the Pyramid
26 Station data. This reanalysis dataset provides 6-hour meteorological data and was resampled
27 using a linear interpolation such that the temporal resolution of the incoming longwave radiation
28 agreed with the half-hour debris temperature measurements.

29 Ablation rates were modeled over the same time period as the ablation stakes (18 May to 09
30 November). For days where no meteorological data was available, i.e., the data gaps, the
31 ablation for that day was assumed to be equal to the daily ablation rate for that specific month.

1 As the available meteorological data began on 31 May, the daily ablation rate for the month of
2 May was assumed to be equal to the daily ablation rate of the first week of June. Temperature
3 sensors revealed the debris was snow covered from 26 May to 01 June, so the melting during
4 these days was assumed to be zero. Temperature profiles also show the debris was snow covered
5 from 13-20 October and deeper thermistors revealed the temperature remained around freezing
6 until the sensors were removed in November. Therefore, the melt rates after the 12 October were
7 assumed to be zero.

8

9 **3 Methods**

10 **3.1 Surface roughness (z_0)**

11 Structure from Motion (SfM) was used to derive fine-resolution (i.e. centimetric) digital
12 elevation models (DEMs) at four sites (Sites A-D) located on the debris-cover of Imja-Lhotse
13 Shar glacier (Figure 2). In brief, SfM relies upon the acquisition of a series of overlapping
14 images that capture the features of the terrain from a number of different vantage points.
15 Computer vision techniques detect matching features between images using multiscale image
16 brightness and colour gradients and a highly iterative bundle adjustment procedure is used to
17 develop a three-dimensional structure of the surface (Snavely et al., 2008). Camera positions
18 and orientations are solved simultaneously with surface geometry utilizing the high level of
19 redundancy afforded by a large overlapping image set. Ground control points (GCPs), collected
20 using a total station with an error less than 0.4 mm, are then used to transform the relative three-
21 dimensional surface into an absolute coordinate system. The resulting point-cloud data are
22 comparable in both density and accuracy to those generated by terrestrial laser scanning
23 (Westoby et al., 2012) and can either be used as-is, or decimated (as in this study) to generate
24 gridded elevation data. The use of SfM within geoscience is well reviewed by Westoby et al.
25 (2012) and specific details of the mathematical operations involved can be found in Snavely
26 (2008) and Szeliski (2011). Here, we therefore focus mostly on our field method and subsequent
27 roughness analysis.

28 At each of our sites ~40 photos were taken around a roughly 2 m x 2 m grid. Cones were placed
29 in the four corners of the grid as GCPs and their location was measured using a total station with

1 a local coordinate system. The GCPs and photos were processed using Agisoft PhotoScan
2 Professional Edition Version 1.1.0 to create a DEM for each site. At each stage, the highest
3 accuracy settings were chosen. No *a-priori* information about camera position or orientation was
4 recorded, so these were estimated coincidentally as part of the adjustment. In each case the
5 initial estimates of camera position and altitude were accepted and used to generate a sparse
6 point cloud ($10^3 - 10^4$ points). A moderate depth filter was then used to derive a dense cloud
7 ($10^6 - 10^7$ points), and subsequently a mesh was constructed using the height field as the surface
8 type. The error of the DEM was computed as the root mean square error based on the
9 differences between the measured GCPs from the total station and the modeled position of the
10 GCPs from the software. The resulting DEMs were then resampled in ArcGIS 10.3 to a
11 resolution of 0.01 m and were clipped to remove the cones from the subsequent analyses. The
12 DEM was then fit with an x-y plane using a method of least squares such that the DEM was
13 flattened with a mean elevation of zero.

14 These processed DEMs of the four sites were analyzed to determine the surface roughness, z_0 .
15 Lettau (1969) developed an empirical relationship to estimate z_0 :

16

$$17 \quad z_0 = 0.5h^* \frac{s}{S} \quad (1)$$

18

19 where h^* is the average vertical extent or effective obstacle height, s is the silhouette area or area
20 of the upwind face of an average element, and S is the specific area or unit ground area occupied
21 by each obstacle. Previous studies have estimated the variables in Equation 1 through a
22 simplified standard deviation approach (which will be referred to as the Lettau-Munro method),
23 based on the variations in elevations and the number of continuous positive groups above the
24 mean elevation (Munro, 1989; Rees and Arnold, 2006; Brock et al., 2006). Initially, the Lettau-
25 Munro method was applied to measure z_0 for every row and column transect of the four DEMs;
26 however, the resulting values of z_0 did not capture the variations between sites and may have
27 been slightly underestimated (see results).

28 Consequently, an alternative method was developed to estimate the effective height, silhouette
29 area, and unit ground area of each obstacle using a similar transect approach and taking

1 advantage of the high resolution DEM. One problem with applying the method from Lettau
2 (1969) is the lack of a clear definition of what constitutes an obstacle. The surface roughness
3 will greatly vary depending on what is considered to be an obstacle, so a method must be
4 developed that (i) objectively determines the obstacle height and (ii) yields reasonable estimates
5 of surface roughness regardless of the resolution of the DEM. Smith (2014) states that the
6 relationship developed by Lettau (1969) holds at low roughness densities (< 20-30% of the
7 surface area), beyond which the observed z_0 is less than that predicted by Lettau (1969) because
8 the obstacles begin to aerodynamically interfere with one another. Therefore, a method was
9 developed to select an obstacle height based on an obstacle density of 30%.

10 Initially, all the relative topographic highs and lows were identified. This was done for all of the
11 transects in each of the four cardinal directions with respect to the DEM, i.e., every East-West,
12 North-South, West-East, and South-North transect. Every elevation change between a relative
13 low and high was considered a potential obstacle. The depth of each obstacle was defined as the
14 distance between two low points surrounding the obstacle's high point. In the event that an
15 obstacle was identified, but there was no low point following the high point, i.e., the low point
16 was outside the extent of the transect, then the depth of the obstacle could not be determined.
17 Figure 3 shows an example of a transect from Site B, which identifies the obstacle's height and
18 depth based on the method developed in this study. The obstacle density was then defined as the
19 cumulative depth of all the obstacles above the obstacle threshold divided by the length of the
20 transect. An iterative approach was then used to determine the obstacle height that causes the
21 obstacle density to reach the 30% threshold.

22 Once the obstacle height has been determined, the silhouette area and unit ground area were
23 approximated from the height and depth of the obstacles. Specifically, the silhouette area was
24 taken to be the height of the obstacle times a unit width and the unit ground area was estimated
25 as the depth of the obstacle times a unit width. Based on these definitions, Equation 1 may be
26 simplified to (Eqn 2):

27

$$28 \quad z_0 = 0.5 \frac{h^{*2}}{d_{obst}^*} \quad (2)$$

29

1 where d_{obst}^* is the average depth of the obstacle. The surface roughness, z_0 , was computed using
2 the average effective obstacle height and average obstacle depth for each transect. In the event
3 that an obstacle was identified, but did not have a depth, the obstacle's height was still used in
4 the average.

5 **3.2 Debris-Covered Glacier Energy Balance Model**

6 The model used in this study was a steady-state surface energy balance model for a debris-
7 covered glacier, where:

$$8 \quad R_n(T_s) + H(T_s) + LE(T_s) + P(T_s) + Q_c(T_s) = 0 \quad (3)$$

10

11 where R_n is the net radiation flux, H is the sensible heat flux, LE is the latent heat flux, P is the
12 heat flux supplied by rain, and Q_c is the ground heat flux (all in W m^{-2}). The net radiation and
13 sensible heat fluxes are fully described in Rounce and McKinney (2014); however, in the current
14 study the incoming shortwave radiation was only corrected for the effects of topography as
15 shading could not be considered due to the lack of a high resolution DEM of the glacier.

16 The latent heat flux is difficult to determine without detailed knowledge of the moisture in the
17 debris or the relative humidity at the surface. As the surface relative humidity was unknown, this
18 study has analyzed three methods for estimating the latent heat flux: (1) assuming the debris is
19 dry ($LE = 0$), (2) assuming it is dry unless the relative humidity is 100%, at which point the
20 surface relative humidity is assumed to also be 100% based on the assumption that the water
21 vapor above the surface is well mixed, and (3) assuming the surface is saturated when it is
22 raining. These methods for modeling the latent heat flux will be referred to herein as LE_{Dry} ,
23 LE_{RH100} , and LE_{Rain} , respectively. The reservoir-approach detailed by Collier et al. (2014) and
24 the empirical relationship between debris thickness and wetness (Fujita and Sakai, 2014) were
25 not applied to this study due to the limited amount of knowledge of moisture within the debris
26 and how the debris properties change with respect to depth. The latent heat flux is thus estimated
27 according to Nicholson and Benn (2006):

28

$$1 \quad LE = \left(\frac{0.622 \rho_{air}}{P_0} \right) L_e A u (e_z - e_s) \quad (4)$$

2 where

$$3 \quad A = \frac{k_{vk}^2}{\ln\left(\frac{z}{z_0}\right)\ln\left(\frac{z}{z_0}\right)} \quad (5)$$

4

5 where ρ_{air} is the density of air at standard sea-level pressure (1.29 kg m⁻³), P_0 is the standard air
6 pressure at sea level (1.013 x 10⁵ Pa), L_e is the latent heat of evaporation of water (2.49 x 10⁶ J
7 kg⁻¹), A is a dimensionless transfer coefficient, u is the wind speed collected at a height of 2 m
8 (m s⁻¹), e_z and e_s are the vapor pressures (Pa) at height z , 2 m, and on the surface of the debris,
9 respectively, k_{vk} is von Karman's constant (0.41), and z_0 is the surface roughness.

10 The heat flux due to precipitation was estimated following Reid and Brock (2010):

11

$$12 \quad P = \rho_w c_w w (T_r - T_s) \quad (6)$$

13

14 where ρ_w is the density of water (999.97 kg m⁻³), c_w is the specific heat capacity of water (4.18 x
15 10³ J kg⁻¹ K⁻¹), w is the rainfall rate (m s⁻¹), and T_r is the temperature of rain (K), which was
16 assumed to be equal to the air temperature.

17 The debris layer was broken down into layers of 0.01 m such that the nonlinear temperature
18 profiles in the debris could be captured using a Crank-Nicholson Scheme (Reid and Brock, 2010).

19 The conductive heat flux at the surface and at the debris/ice interface were estimated following
20 Reid and Brock (2010):

21

$$22 \quad Q_{c,s} = k_{eff} \frac{T_d(1) - T_s}{h} \quad (7)$$

$$23 \quad Q_{c,ice} = k_{eff} \frac{T_d(N-1) - T_{ice}}{h} \quad (8)$$

24

1 where k_{eff} is the effective thermal conductivity ($\text{W m}^{-1} \text{K}^{-1}$), h is the height of each layer in the
2 debris set at 0.01 m, and $T_d(1)$, $T_d(N-1)$, T_{ice} are the temperatures (K) of the first layer in the
3 debris, the last layer before the debris/ice interface, and the temperature of the ice (273.15 K),
4 respectively.

5 The surface temperature was computed at half-hour time steps using an iterative Newton-
6 Raphson method approach as detailed in Reid and Brock (2010). In the event of snow, a simple
7 snowmelt model was used (Fujita and Sakai, 2014), which applies an energy balance over the
8 snow surface that includes net radiation, turbulent heat fluxes, and conductive heat flux with the
9 debris layer in addition to a variable surface albedo of the snow based on the number of days
10 since fresh snow and the air temperature. The thermal conductivity of snow was assumed to be
11 $0.10 \text{ W m}^{-1} \text{K}^{-1}$ (Sturm et al., 1997; Sturm et al., 2002; Rahimi and Konrad, 2012) and the surface
12 roughness of the snow was assumed to be 0.002 m (Brock et al., 2006). If snow was on the
13 surface, all the heat fluxes at the debris surface were assumed to be zero with the exception of
14 the conductive heat flux in the debris and at the debris/snow interface. If all the snow was
15 melted on the surface, then the next time step returned to the snow-free energy balance model.

16 As detailed knowledge of albedo, thermal conductivity, and surface roughness was not available
17 for the sites where temperature sensors were installed, the debris-covered glacier energy balance
18 model was calibrated at each site from 02 June to 30 July 2014. The calibration was performed
19 by minimizing the total sum of squares of the measured versus modeled surface temperature for
20 each site and was done independently for the three methods used to estimate the latent heat flux.
21 Bounds for the thermal conductivity and surface roughness were based on measured field data
22 (see results), while the bounds for the albedo were 0.1 – 0.4 (Inoue and Yoshida, 1980; Kayastha
23 et al., 2000; Nicholson and Benn, 2012; LeJeune et al., 2013). A validation was then conducted
24 at each site using data from 08 August to 12 October 2014 to assess how well the calibrated
25 model performed.

26

1 **4 Field results**

2 **4.1 Thermal Conductivity (k)**

3 The thermal conductivity, k , of the debris was computed using the temperature measurements
4 from Sites 4, 11, and 13 over the time period of the study (02 June – 12 October 2014) following
5 the methods of Conway and Rasmussen (2000). The calculations used standard values for the
6 density of rock (2700 kg m^{-3}), volumetric heat capacity of rock ($750 \text{ J kg}^{-1} \text{ K}^{-1} \pm 10\%$), and
7 effective porosity (0.33) based on Nicholson and Benn (2012). Depending on the vertical
8 spacing of temperature sensors at a site, k was computed at depths of 0.05, 0.10, and 0.20 m.
9 The values of thermal conductivity ranged from 0.42 (± 0.04) to 2.28 (± 0.23) $\text{W m}^{-1} \text{ K}^{-1}$. The
10 average value of k for each site was 1.44 (± 0.14), 1.62 (± 0.16), and 0.47 (± 0.04) $\text{W m}^{-1} \text{ K}^{-1}$ for
11 Sites 4, 11, and 13, respectively.

12 These values agree well with other studies in the Everest region that have found the thermal
13 conductivity to vary between 0.60 to 1.29 $\text{W m}^{-1} \text{ K}^{-1}$ (Conway and Rasmussen, 2000; Nicholson
14 and Benn, 2012; Rounce and McKinney, 2014). In September 2013, Rounce and McKinney
15 (2014) found the thermal conductivity to be greatly influenced by depth; however, this trend was
16 not apparent in our current data. We believe this disparity can be explained by the time period
17 during which the data were collected. It is likely that the temporally-limited data (13-24 Sept
18 2013) presented in Rounce and McKinney (2014) represent a constantly dry surface, whereas
19 here we observed an entire melt season, where the surface is exposed to precipitation and snow.
20 The thermal conductivities appeared to have a trend over the monsoon season where the highest
21 thermal conductivities were typically observed in July and August, which coincided with higher
22 average air temperature and increased precipitation compared to the other months. As k_{eff} is one
23 of the parameters that is used to calibrate the model, the range of average thermal conductivity
24 ($0.47 - 1.62 \text{ W m}^{-1} \text{ K}^{-1}$) will be used to bound k_{eff} .

25 **4.2 Surface roughness (z_0)**

26 The DEMs generated using the SfM workflow had a total root mean square error of 0.008 –
27 0.024 m. Table 2 shows that the errors in elevation (i.e., z) were smaller than in planform (i.e., x
28 and y) with a maximum error of 0.007 m. The contrast between elevation and planimetric errors
29 is likely a result of the identification of the GCPs in each photo during the SfM workflow, since

1 it was easier to identify the top of the cone in each photo than it was to determine the exact point
2 on the rim of the cone. As the error with the total station is small (maximum of 0.4 mm), this
3 human error likely dominated the total error, although errors in estimates of both camera position
4 and orientation will also have contributed. The DEMs were resampled to a resolution of 0.01 m
5 such that their resolution was on the same order as their respective errors (3 of the 4 sites had a
6 total RMSE less than 0.01 m). The DEMs were then de-trended to account for variations in the
7 local topography.

8 Initially, z_0 was estimated from Equation 1 using the Lettau-Munro method. The average value
9 of z_0 was 0.0037, 0.0091, 0.0022, and 0.0033 m for Sites A, B, C, and D, respectively. These
10 values are towards the lower end of those previously reported in literature, which were estimated
11 from wind speed profiles and range from 0.0035 to 0.060 m (Inoue and Yoshida, 1980; Takeuchi
12 et al., 2000; Brock et al., 2010). In particular, the average value of z_0 for Sites A, C, and D was
13 comparable or smaller to Area IV on the Khumbu glacier (Inoue and Yoshida, 1980), which
14 comprised small schist with bare ice. Sites A, C, and D were all debris-covered with boulders
15 ranging up to 0.40 m, so these small estimations of z_0 are concerning. Site B also appears to be
16 underestimated as it has similar debris characteristics to Area III on the Khumbu glacier (Inoue
17 and Yoshida), yet its average value of z_0 was much smaller (0.0091 m compared to 0.060 m,
18 respectively). These apparent underestimations of z_0 led to the development of an alternative
19 method.

20 The alternative method relies upon the selection of the obstacle height (or threshold) such that
21 the obstacle density is 30% (Smith, 2014). Figure 4 shows that as the obstacle threshold is
22 increased, the obstacle density decreases, which makes intuitive sense as there will be fewer
23 obstacles in the transect. Table 3 shows the values of z_0 using an obstacle density of 30% and
24 the highest resolution DEM (0.01 m) were 0.016, 0.043, 0.006, and 0.014 m for Sites A-D,
25 respectively. These values agree well with the range of z_0 values previously reported (Inoue and
26 Yoshida, 1980; Takeuchi et al., 2000; Brock et al., 2010). Furthermore, these z_0 values appear to
27 capture the inter-site variability as Site B had the highest value of z_0 (0.043 m), which is expected
28 since the debris cover includes large boulders up to 1 m in size (Figure 2). Site C, which
29 comprised the smallest grain sizes of the four sites in this study had the lowest estimation of z_0
30 (0.006 m). Sites A and D had similar values of surface roughness and the standard deviations of

1 Site A and D (0.008 m and 0.012 m, respectively) appear to capture the more homogenous
2 surface of Site A compared to the highly heterogeneous surface of Site D (Figure 2).

3 The impact of DEM resolution on obstacle threshold and z_0 was analyzed to determine the
4 robustness of this alternative method. Since the terrain is not changing and only the sampling
5 frequency is varying, the z_0 values should remain fairly constant. Table 3 shows that the obstacle
6 threshold increases as the resolution of the DEM becomes coarser. This occurs because the
7 coarser resolution cannot capture the subtler changes in surface height over the debris cover. On
8 the other hand, the estimations of z_0 remain relatively constant (± 0.004 m) as the DEM
9 resolution is reduced to 0.04 m. The consistency of this method despite variations in DEM
10 resolution and obstacle thresholds, and the objective approach for deriving the obstacle threshold
11 using a 30% obstacle density lends confidence to this method. Furthermore, Nield et al. (2013b)
12 found that measures regarding surface heights are the best predictor of aerodynamic roughness,
13 specifically for surfaces that comprise large elements or have patches of large and small elements.
14 Therefore, it is expected that the obstacle threshold should vary for different sites as a function of
15 their largest elements, which is consistent with the inter-site variability and the obstacle
16 thresholds reported in this study.

17 **4.3 Ablation Stakes**

18 Ablation stakes were installed on 18-19 May 2014 approximately 1 m into the ice at 14 sites with
19 debris thicknesses ranging from 0.07 to 0.54 m (Table 1). The ablation stakes were measured on
20 09 November 2014. At 11 of the 14 sites, the ablation stakes completely melted out of the ice
21 indicating there was greater than 1 m of ablation. Sites 8, 13, and 15, had ablation measurements
22 of 0.92, 0.85, and 0.89 m, respectively. These three sites had debris thicknesses of 0.20, 0.33,
23 and 0.37 m and were oriented in the southern, northeast, and northwest directions, respectively.
24 The lower ablation rates of Sites 13 and 15 compared to the other 12 sites is likely due to a
25 combination of their debris thickness and aspect as they are oriented in a manner that receives
26 less solar radiation throughout the day. Site 8 appears to be an anomaly as it has a smaller debris
27 thickness than 8 of the sites with ablation stakes and a southerly aspect, which positions it in a
28 manner to receive a greater amount of solar radiation throughout the day. It is possible that Site
29 8 had a higher albedo and/or a lower thermal conductivity, which would greatly reduce its
30 ablation; unfortunately, these properties could not be measured in the field. Nevertheless, the

1 ablation measurements indicate that understanding ablation rates on debris-covered glaciers is
2 greatly influenced by slope, aspect, and properties of the debris (albedo, thermal conductivity,
3 and surface roughness).

4

5 **5 Modeled Results**

6 **5.1 Model Calibration**

7 Three different methods were used to estimate the latent heat flux to determine how well each
8 method models the measured debris temperatures. These methods are referred to as LE_{Rain} ,
9 LE_{RH100} , and LE_{Dry} . The albedo, thermal conductivity, and surface roughness for each of the
10 three methods were optimized by minimizing the sum of squares of the surface temperature for
11 each site (Table 4). For the LE_{Rain} and LE_{RH100} model, 7 of the 10 sites had a thermal
12 conductivity at the upper bound ($1.62 \text{ W m}^{-1} \text{ K}^{-1}$), while for the LE_{Dry} model 9 of the 10 sites
13 were at the upper bound. These results indicate that the selection of the upper bound for the
14 thermal conductivity is important and its impact on model performance is detailed in the
15 discussion section. The albedo values ranged from 0.10 – 0.40 and had an average value around
16 0.32, which is consistent with albedos measured in the Khumbu (Inoue and Yoshida, 1980;
17 Kayastha et al., 2000; Nicholson and Benn, 2012; LeJeune et al., 2013). The values of z_0 had an
18 average around 0.014 m, which is consistent with z_0 measured in this study and those reported on
19 other debris-covered glaciers (Inoue and Yoshida, 1980; Takeuchi et al., 2000; Brock et al.,
20 2010). For the LE_{Rain} and LE_{RH100} models, 5 of the 10 sites had a value of z_0 at its lower bound
21 (0.006 m), which highlights the importance of measuring the surface roughness of the debris
22 cover and will be discussed in the sensitivity analysis.

23 The performance of each model was assessed using the total sum of squares and the R^2
24 correlation coefficients. The R^2 values ranged from 0.34 to 0.92 for all three models. The
25 average R^2 values over the calibration period for the LE_{Rain} , LE_{RH100} , and LE_{Dry} models were 0.72,
26 0.72, and 0.71, respectively. Figures 5C and 5D show the correlation between the modeled and
27 measured surface temperature at Site 11, which had an R^2 of 0.77 and 0.75 for the calibration and
28 validation periods, respectively. Figure 5C shows there is good agreement between the modeled
29 and measured temperature sensors. The modeled temperatures appear to capture the daily

1 variations in temperature well. However, there are a few days for which a positive bias in
2 temperature can be seen during the daily high and nightly low (e.g., Figure 5C from 16-18 June
3 and 25-27 July). Interestingly, the overestimation of the daily high typically occurs after the
4 nightly low has a positive bias in temperature during the previous night. The positive bias of the
5 nightly minimum is apparent between the hours of 0:00 and 6:00 (Figure 6). One possible
6 explanation for the positive bias in temperature in the nightly low is an overestimation of the
7 incoming longwave radiation due to the poor temporal and spatial resolution of the
8 NCEP/NCAR reanalysis dataset compared to the other meteorological data from Pyramid Station.
9 Typically, the wind speed during the night is relatively low thereby limiting the turbulent heat
10 fluxes, which causes the incoming longwave radiation to be a major source of energy during this
11 time.

12 Nonetheless, the model performs reasonably well for all of the temperature sensors.
13 Unfortunately, it is difficult to determine which latent heat flux model performs the best using
14 the total sum of squares and/or the R^2 values as there was not one particular model that
15 consistently had a lower total sum of squares and/or a higher R^2 at each site. The average R^2
16 value was fairly comparable for all three models. The total sum of squares of all the sites was
17 the lowest for the LE_{RH100} model followed by the LE_{Rain} model and then the LE_{Dry} model, but the
18 difference between models was less than 5%.

19 **5.2 Model Validation**

20 Model validation was assessed from 08 August to 12 October 2014 for all three models using the
21 R^2 values for each temperature sensor. The R^2 values for all the temperature sensors at the 10
22 sites ranged from 0.39 to 0.81 for all three methods. The average R^2 value for the LE_{Rain} ,
23 LE_{RH100} , and LE_{Dry} was 0.67, 0.67, and 0.68, respectively. Again, the similar performance
24 between the three models does not provide any insight into preference for one model and is
25 likely a result of the calibration procedure. Figure 5D shows that the LE_{Rain} model performs well
26 through the entire validation period. Similar to the calibration period, the LE_{Rain} model appears
27 to underestimate the nightly low, which causes the following daily high to be overestimated.

28 Reid and Brock (2010) found R^2 values of 0.94 and 0.52 for temperature sensors at the surface
29 and at a depth of 15 cm, respectively. While the R^2 value of 0.94 is higher than those found in
30 this study, the range of R^2 is comparable. In contrast to the findings of Reid and Brock (2010),

1 the average R^2 value for the surface temperature sensors (0.67-0.68 for all three models) was
2 very similar to the average R^2 value of those buried in the debris (0.66-0.68 for all three models).
3 The slightly lower R^2 values in this study may be a result of using meteorological data from an
4 AWS located 14 km away from the glacier. Furthermore, longwave radiation was estimated
5 from remotely sensed data, which may also influence model performance as previously
6 discussed.

7 **5.3 Modeled Ablation Rates**

8 Ablation rates were computed for all 15 sites that had a temperature sensor or an ablation stake.
9 For sites that only had an ablation stake, the average calibrated parameters for that particular
10 latent heat flux model were used. Additionally, ablation rates were estimated for the LE_{Rain}
11 model using the average calibrated parameters for all the sites to assess the differences between
12 using a single set of parameters compared to optimizing the parameters at each site. The
13 modeled ablation over the entire duration of the study period varied from 0.39 to 2.85 m among
14 the three methods (Figure 7). On average the LE_{Dry} model overestimated both the LE_{Rain} and
15 LE_{RH100} models by 7.9%. The slight variations in ablation between the models are directly
16 related to the differences in their calibrated parameters. The slightly higher ablation rates for the
17 LE_{Dry} model is likely attributed to the higher values of thermal conductivities and the lack of a
18 latent heat flux term to remove heat from the debris. Figure 7 shows there is a clear relationship
19 between debris thickness and ablation as thin debris has higher rates of ablation compared to
20 thicker debris, which insulates the ice to a greater extent thereby retarding ablation. The scatter
21 found throughout the curve, specifically between 0.25 and 0.50 m, is due to the site-specific
22 debris properties and the slope and aspect of each site. A comparison between the LE_{Rain} model
23 using the optimized parameters at each site and those using the average calibrated parameters at
24 each site highlights the effect that site-specific properties has on ablation. Site 6, with a debris
25 thickness of 0.08 m, is a good example as the use of average calibrated parameters increased the
26 melt from 2.03 m to 2.70 m due to an increase in thermal conductivity from $1.29 \text{ W m}^{-1} \text{ K}^{-1}$ to
27 $1.52 \text{ W m}^{-1} \text{ K}^{-1}$. These differences in melt and the sensitivity to thermal conductivity highlight
28 the importance of properly estimating/measuring the thermal conductivity of the debris cover.

29 The modeled ablation rates may also be compared to the measured ablation rates. Specifically,
30 Sites 8, 13, and 15 had measured ablation rates of 0.92, 0.85 and 0.89 m compared to their

1 modeled ablation rates of 1.76, 0.76, and 1.22 m, respectively, for the LE_{Rain} model. The large
2 discrepancy between the measured and modeled ablation rates at Site 8 may be due to the lack of
3 knowledge of the debris properties at Site 8 as previously discussed. The difference between the
4 modeled and measured ablation rates at Site 15 may also be a result of the thermal conductivity
5 parameter ($1.61 \text{ W m}^{-1} \text{ K}^{-1}$), which is slightly higher than thermal conductivities previously
6 reported in the Khumbu, which ranged from 0.60 to $1.29 \text{ W m}^{-1} \text{ K}^{-1}$. A comparison of the daily
7 average temperatures for Site 15 reveals there was about an hour lag between the modeled and
8 measured temperatures (results not shown). Lags between temperatures are typically a result of
9 their depth (Conway and Rasmussen, 2000), which is apparent in Figure 5A as the 0.10 m sensor
10 lags behind the 0.01 m sensor. It is possible that debris may have shifted over the melt season
11 causing the measured temperature to be at a lower depth than 0.01 m, which would greatly
12 influence the model calibration and potentially cause the thermal conductivity to vary. Site 5
13 was the only other site where a slight lag was observed between the measured and modeled
14 temperatures. The modeled ablation at Site 5 was 0.87 m using the LE_{Rain} model, while the
15 ablation stake melted completely out of the ice indicating greater than 1 m of ablation. All the
16 other model estimates of ablation were near to or greater than 1 m, which was also observed by
17 their respective ablation stakes as they completely melted out of the ice.

18 The ablation results also show strong seasonal trends with maximum melt rates occurring in June,
19 July, and August. These ablation rates appear to taper off towards the transition seasons. Melt
20 rates in July and August ranged from $0.3 - 2.5 \text{ cm day}^{-1}$ based on the debris thickness, which is
21 consistent with empirical relationships between mean daily ablation rate and debris thickness
22 found on other glaciers (Nicholson and Benn, 2006). The total ablation rates are also similar to
23 those measured on Imja-Lhotse Shar glacier using multiple DEMs, which were $1.45 \pm 0.52 \text{ m yr}^{-1}$
24 (Bolch et al., 2011), thereby lending confidence to the results.

25 **5.4 Sensitivity Analysis**

26 A sensitivity analysis was performed to assess how albedo, thermal conductivity, and surface
27 roughness affect the total ablation (Table 5) based on the uncertainty with respect to each
28 parameter. The uncertainty in thermal conductivity was $\pm 0.40 \text{ W m}^{-1} \text{ K}^{-1}$ as described above.
29 The uncertainty associated with the surface roughness was $\pm 0.010 \text{ m}$, which is the approximate
30 standard deviation associated with the z_0 values for each of the three models (Table 4) and

1 similar to the standard deviation between the four sites where z_0 was measured (± 0.016 m).
2 Lastly, the uncertainty of the albedo was estimated as ± 0.10 , which is the approximate standard
3 deviation within the model calibration for each of the three models and also the difference
4 between the mean and median albedo measured by Nicholson and Benn (2012) on Ngozumpa
5 glacier. The LE_{Rain} model was used as the baseline case and the average value for each of the
6 calibrated parameters (α , k , z_0) from the model optimized is used for each site.

7 Table 5 shows the total ablation is most sensitive to changes in the thermal conductivity, where a
8 $\pm 0.40 \text{ W m}^{-1} \text{ K}^{-1}$ change causes a $\pm 20.5\%$ change in total ablation on average. The uncertainty
9 associated with the thermal conductivity is also more sensitive to thicker debris, which is
10 consistent with the findings of Nicholson and Benn (2012). Total ablation is also moderately
11 sensitive to changes in the albedo, where a ± 0.10 change causes a $\pm 12.0\%$ change in total
12 ablation. Lastly, the total ablation is least sensitive to changes in increasing the surface
13 roughness, as a $+0.010$ m increase in z_0 only caused a -7.3% change in total ablation. However,
14 the model was quite sensitive to a reduction in the z_0 of -0.010 m, which caused an average
15 change in total ablation of $+15.0\%$. The sensitivity associated with z_0 also appears to increase
16 with an increase in debris thickness. These results highlight the importance of properly
17 estimating the thermal conductivity, but also show the surface roughness and the albedo are
18 important as well.

19 **5.5 Temporal Resolution**

20 Nicholson and Benn (2006) proposed that the temperature gradient in the debris may be assumed
21 to be linear at a time step greater than a day, but is nonlinear for shorter time steps. This would
22 have important implications for modeling melt on remote debris-covered glaciers where
23 meteorological data is not available and reanalysis datasets could be used instead. The
24 importance of temporal resolution was analyzed using 6-hour and daily average data from
25 Pyramid Station, which are consistent with the temporal resolution of NCEP/NCAR reanalysis
26 datasets. To be consistent with this reanalysis dataset such that only the effects of temporal
27 resolution were analyzed, the wind speed and relative humidity used were instantaneous values
28 from Pyramid Station, while all the other variables were 6-hour averages. For the daily time step,
29 all the parameters were daily averages and the temperature profile in the debris is assumed to be
30 linear. The LE_{Rain} model was used to model the latent heat flux.

1 The R^2 correlation coefficients for the sites with temperature sensors and the modeled total melt
2 for all 15 sites were used to assess the effect of temporal resolution on model performance. The
3 R^2 using the 6-hour data ranged from 0.30 to 0.80 with an average of 0.55 over the calibration
4 period and was significantly poorer during the validation period with R^2 values ranging from
5 0.15 to 0.65 with an average of 0.35. Figure 8A shows the surface temperature at Site 11 does
6 fairly well ($R^2 = 0.63$) at modeling the measured surface temperatures over the calibration period.
7 The lower R^2 values compared to the 30 minute time step appears to be a result of the 6-hour
8 model underestimating the daily high, which occurs around 15:00 each day. Furthermore, Figure
9 8B shows the 6-hour model poorly replicates the measured data towards the transition seasons
10 when snowfall becomes significant, which explains the poorer R^2 values for the validation period.
11 Snowfall is problematic in the model for large time steps because the model assumes the snow is
12 on the surface for the entire time step. Therefore, a small snow event that could melt quickly on
13 the debris and then allow the debris to warm up during the day is perceived to remain on the
14 snow for the 6-hour time step (e.g., Figure 8B from 27 Sept to 03 October). The same problem
15 arises at the daily time step, so a snow-free model was used instead. For the daily time step, the
16 R^2 values ranged from 0.18 to 0.63 with an average of 0.29. Figure 8C shows the daily time step
17 is able to capture some of the temperature fluctuations over the melt season, but does not
18 perform as well as the 30-minute or 6-hour models.

19 Since we are most interested in understanding the effects of temporal resolution, the 6-hour data
20 and daily averages from 02 June to 25 September 2014 were assessed, which is prior to the time
21 when snowfall was recorded each day. A comparison of all the modeled and measured
22 temperatures at the surface reveals the 6-hour model underestimates the measured temperatures
23 by an average of 1.0 (± 4.3) K over the entire time period. The modeled total ablation from 02
24 June to 25 September reveals the ablation is consistently underestimated at all sites by an
25 average of 11 (± 5) %. The lower estimates of ablation are likely a result of the underestimation
26 of the daily high as previous discussed. Similar to the 6-hour model, the daily time step model
27 slightly underestimates the measured temperatures at the surface on average by 0.3 (± 1.9) K.
28 The modeled total ablation is also underestimated by an average of 6 (± 10) %. However, it is
29 important to note that 5 of the 15 sites are actually slightly overestimated the melt. These results
30 suggest that if high-temporal meteorological data are not available, a first-order estimate of
31 ablation over a melt season could be obtained using the daily time step model. It is important

1 that the estimate is made over the entire melt season, as the daily model does not capture the
2 daily temperature fluctuations well. Furthermore, caution should be used to avoid the transition
3 seasons as both the daily model and the 6-hour model do not have a small enough time step to
4 properly account for snow melt.

5

6 **6 Discussion**

7 **6.1 Thermal Conductivity**

8 One of the limitations with regards to the thermal conductivity measurements is that all the
9 measurements were made near the surface. Therefore, the estimates of the average thermal
10 conductivity at each site are potentially underestimated because the deeper layers that may be
11 more compact and humid are not considered. The lack of any trends with respect to depth
12 appears to dispute this theory; however, this is based on a limited number of measurements near
13 the surface. Interestingly, the thermal conductivities measured at Sites 4 and 11 are similar to
14 those estimated by Nicholson and Benn (2012) for debris cover on Ngozumpa glacier with 10%
15 and 20% of the void space being filled with water (1.42 and $1.55 \text{ W m}^{-1} \text{ K}^{-1}$, respectively).

16 The number of sites that reached the upper bound during the model calibration is concerning as it
17 may indicate that the actual thermal conductivity throughout the debris is higher. To address this
18 issue, an additional calibration was performed allowing the thermal conductivity to be
19 unbounded. This calibration revealed that 3 or more out of the 10 sites for each method had
20 thermal conductivities greater than $3.0 \text{ W m}^{-1} \text{ K}^{-1}$ with one thermal conductivity as high as 4.5 W
21 $\text{m}^{-1} \text{ K}^{-1}$. The lithology of the debris cover in the Everest region is predominantly granite, gneiss,
22 and pelite (Hambrey et al., 2008). Robertson (1988) found the thermal conductivity of solid
23 granite gneiss to be $2.87 \text{ W m}^{-1} \text{ K}^{-1}$, so the unbounded thermal conductivities do not appear to
24 make physical sense when one considers that the thermal conductivity of debris should be much
25 lower than solid rock due to the pore spaces being filled with air and water. Furthermore, an
26 optimization performed using the total sum of squares of all the surface sites reveals that
27 increasing the thermal conductivity from $1.6 \text{ W m}^{-1} \text{ K}^{-1}$ to its minimum of $2.6 \text{ W m}^{-1} \text{ K}^{-1}$ only
28 reduces the total sum of squares by 3%. These results and the similar values to Nicholson and
29 Benn (2012) lend confidence to the use of $1.62 \text{ W m}^{-1} \text{ K}^{-1}$ as the upper bound, but highlights the

1 importance of understanding how the moisture varies within the debris and its influence on the
2 thermal conductivity. Future work should improve measurements of the thermal conductivity by
3 a) accurately measuring the depth of the temperature sensors during installation and retrieval, b)
4 installing additional sensors (e.g. 5 cm spacing) that allow thermal conductivity within the debris
5 to be computed at more depths, and c) measuring moisture in the debris at various depths.

6 **6.2 Surface Roughness**

7 The development of an alternative method for estimating z_0 was required, as the Lettau-Munro
8 method appeared to greatly underestimate the values of z_0 . The alternative method applies the
9 relationship developed by Lettau (1969) to a high resolution DEM using the selection of an
10 obstacle height (threshold) based on an obstacle density of 30%. One of the main limitations of
11 this study is the lack of aerodynamic roughness measurements to validate the developed methods.
12 Previous work, e.g., Rees and Arnold (2006), has relied upon surface roughness estimates from
13 other studies to assess the reasonableness of their results when aerodynamic data were not
14 collected. This study relies upon the results of Inoue and Yoshida (1980), which estimated
15 surface roughness using wind speed profiles at two sites on the Khumbu glacier. Specifically,
16 Sites B and C in this study have similar debris cover to Areas III and IV from Inoue and Yoshida
17 (1980), respectively.

18 Site B had the highest value of z_0 (0.043 m) of the four sites in this study and consisted of larger
19 boulders up to 1 m in size. This value is similar to the higher value of 0.060 m for z_0 derived
20 from a region on the Khumbu glacier that consisted of large granitic boulders of 1-2 m in size
21 lying on top of schistose rocks with a grain size varying from a few centimeters to 0.5 m (Inoue
22 and Yoshida, 1980). The larger boulders observed by Inoue and Yoshida (1980) may explain the
23 slightly higher value of z_0 compared to Site B. Site C, which comprised the smallest grain sizes
24 of the four sites in this study, agrees well with the smaller value of z_0 (0.0035 m) derived by
25 Inoue and Yoshida (1980) for an area where the supraglacial debris comprised dispersed
26 boulders ranging in size of 0.01 – 0.05 m. The few boulders ranging in size of up to 0.15 m may
27 be the reason for Site C's slightly larger value of z_0 (0.006 m). Sites A and D were composed of
28 boulders and grains that varied in size between those found in Sites B and C; therefore, we deem
29 the value of z_0 of 0.016 and 0.014 m for Sites A and D, respectively, to be reasonable.
30 Furthermore, these values agree fairly well with the z_0 of 0.016 m measured by Brock et al.

1 (2010) on a debris-covered glacier in Italy that comprised a mixture of granites and schists of
2 predominantly cobble size, with occasional boulders of < 1 m size.

3 Future work should seek to compare these estimates of surface roughness with aerodynamic
4 roughness to determine the scale at which these two values agree. Brock et al. (2006) found
5 there to be no significant difference between the use of a 3 m and 15 m transect; however, they
6 did state that a shorter pole would be unlikely to capture a sufficient sample of roughness
7 elements if the vertical changes are greater than 1 m. The use of hundreds of transects over a ~4
8 m² grid has the benefit of expanding the number of surface roughness elements that can be
9 captured compared to a single transect. However, Brock et al. (2006) was comparing
10 microtopographic and aerodynamic roughness over snow, slush, and ice, which is significantly
11 different from the hummocky and heterogeneous terrain on debris-covered glaciers. Therefore, it
12 will be important to determine the scale or fetch length at which the surface roughness agrees
13 with the aerodynamic roughness. Nonetheless, the method developed in this paper provides an
14 objective approach to select an obstacle height and yields consistent and reasonable estimates of
15 z_0 for various grain sizes independent of the resolution of the DEM.

16 **6.3 Modeled Results**

17 One of the limitations of the calibration procedure is the LE_{Rain} , LE_{RH100} , and LE_{Dry} models all
18 performed reasonably well. The lack of a single model clearly outperforming the others
19 indicates that either a) the modeling of the latent heat flux is insignificant or b) the latent heat
20 flux is significant, but the calibration procedure allows for changes in the latent heat flux to be
21 compensated for via other model parameters. Brock et al. (2010) found that latent heat fluxes
22 may be a significant energy sink when rain falls on warm debris indicating that the latent heat
23 flux is important to include. They also assessed the importance of each component of the energy
24 balance and found that inclusion of the latent heat flux improved the correlation coefficient of
25 their model. The average latent heat flux for both the LE_{Rain} and LE_{RH100} models were
26 comparable with values ranging from -53 to 10 W m⁻² over the day. The peak instantaneous
27 latent heat fluxes varied greatly between the two models with fluxes as high as -714 and -323 W
28 m⁻², for the LE_{Rain} and LE_{RH100} models, respectively. These values are similar to those reported
29 by Brock et al. (2010) and support the importance of including the latent heat flux term.
30 However, they do not yield any insight into preference between the LE_{Rain} or LE_{RH100} models.

1 These results suggest that the selection of the LE_{Rain} or LE_{RH100} model should be based on data
2 availability. Future work should seek to measure the thermal conductivity, albedo, and surface
3 roughness, which would allow the differences between models to be evaluated. Furthermore,
4 detailed knowledge of the debris properties, including how the thermal conductivity and water
5 content vary with depth, would allow the performance of these models to be compared to other
6 debris-covered glacier energy balance models (Collier et al., 2014; Fujita and Sakai, 2014).

7

8 **7 Conclusions**

9 Debris thickness greatly impacts ablation rates on debris-covered glaciers; however,
10 incorporating debris cover into energy balance models is still hampered by a lack of knowledge
11 of the debris properties. Fieldwork performed on Imja-Lhotse Shar glacier over the 2014 melt
12 season was used to develop new techniques to measure surface roughness, which yielded
13 reasonable values for various grain sizes. Temperature sensors and ablation stakes installed in
14 the debris were also used to assess the performance of a debris-covered glacier energy balance
15 model using three different methods for estimating the latent heat flux. All three models
16 performed well, as a result of the calibration procedure, which allowed variations in the lack of
17 latent heat flux to be compensated for by adjusting the debris properties. However, the LE_{Rain}
18 and LE_{RH100} models yielded more reasonable values of latent heat fluxes. This suggests that in a
19 data-scarce region either the LE_{Rain} or LE_{RH100} model may be used if relative humidity or
20 precipitation data are available.

21 A sensitivity analysis revealed ablation rates were most sensitive to variations in thermal
22 conductivity, followed closely by albedo and surface roughness. This highlights the importance
23 of measuring the thermal conductivity and the moisture content in the debris. The effect of
24 temporal resolution on model performance was also explored using a 6-hour time step and a
25 daily time step. The 6-hour time step was found to underestimate the daily high each day, which
26 caused the ablation rates to also be slightly underestimated. The daily time step did not model
27 the daily average temperature as well, but yielded better estimates of ablation over the entire melt
28 season.

29 Future studies should continue to work on incorporating the water content in the debris into
30 debris-covered glacier energy balance models and determine its effect on thermal conductivity

1 and the latent heat flux. Furthermore, an increased understanding of how the albedo may vary
2 over the course of the day, the course of the melt season, and as a function of debris saturation,
3 may significantly improve model performance. Lastly, the methods developed in this study have
4 the potential to be scaled up such that maps of surface roughness on a whole glacier scale may be
5 developed in the future, but it is imperative to determine the scale at which the surface roughness
6 and aerodynamic roughness agree with one another.

7

8 **Acknowledgements**

9 The authors acknowledge the support of the USAID Climate Change Resilient Development
10 (CCRD) project for the support of Rounce. The meteorological data from Pyramid Station used
11 in this study was collected within the SHARE Project thanks to contributions from the Italian
12 National Research Council and the Italian Ministry of Foreign Affairs. The NCEP Reanalysis
13 data provided by the NOAA/OAR/ESRL PSD, Boulder, Colorado USA from their website
14 <http://www.esrl.noaa.gov/psd/> was also very helpful. We also acknowledge the support of Dr.
15 Dhananjay Regmi of Himalayan Research Expeditions for temperature sensors and logistical
16 support during fieldwork.

17

18 **References**

19 Benn, D.I., Bolch, T., Hands, K., Gulley, J., Luckman, A., Nicholson, L.I., Quincey, D.,
20 Thompson, S., Toumi, R., Wiseman, S.: Response of debris-covered glaciers in the Mount
21 Everest region to recent warming, and implications for outburst flood hazards, *Earth-Science*
22 *Reviews*, 114:156–174, 2012.

23 Bolch, T., Pieczonka, T., and Benn, D.I.: Multi-decadal mass loss of glaciers in the Everest area
24 (Nepal Himalaya) derived from stereo imagery, *The Cryosphere*, 5:349-358, 2011.

25 Brock, B.W., Willis, I.C., and Sharp, M.J.: Measurement and parameterization of aerodynamic
26 roughness length variations at Haut Glacier d’Arolla, Switzerland., *J. Glaciol.*, 52(177):281-297,
27 2006.

28 Brock, B.W., Mihalcea, C., Kirkbride, M.P., Diolaiuti, G., Cutler, M.E.J. and Smiraglia, C.:
29 Meteorology and surface energy fluxes in the 2005–2007 ablation seasons at the Miage debris-

1 covered glacier, Mont Blanc Massif, Italian Alps. *J. Geophys. Res.*, 115, D09106,
2 doi:10.1029/2009JD013224, 2010.

3 Collier, E., Nicholson, L.I., Brock, B.W., Maussion, F., Essery, R., and Bush, A.B.G.:
4 Representing moisture fluxes and phase changes in glacier debris cover using a reservoir
5 approach, *The Cryosphere*, 8:1429-1444, doi:10.5194/tc-8-1429-2014, 2014.

6 Conway, H. and Rasmussen, L.A.: Summer temperature profiles within supraglacial debris on
7 Khumbu Glacier, Nepal, *Debris-Covered Glaciers, Proceedings of a workshop held at Seattle,*
8 *Washington, USA, September 2000.*

9 Foster, L.A., Brock, B.W., Cutler, M.E.J., and Diotri, F.: Instruments and methods: A physically
10 based method for estimating supraglacial debris thickness from thermal band remote-sensing
11 data, *J. Glaciol.*, 58(210):677-691, doi:10.3189/2012JoG11J194, 2012.

12 Fujita, K. and Sakai, A.: Modelling runoff from a Himalayan debris-covered glacier, *Hydrol.*
13 *Earth Syst. Sci.*, 18:2679-2694, doi:10.5194/hess-18-2679-2014, 2014.

14 Fyffe, C.L., Reid, T.D., Brock, B.W., Kirkbride, M.P., Diolaiuti, G., Smiraglia, C., and Diotri,
15 F.: A distributed energy-balance melt model of an alpine debris-covered glacier, *J. Glaciol.*,
16 60(221):587-602, doi:10.3189/2014JoG13J148, 2014.

17 Hambrey, M.J., Quincey, D.J., Glasser, N.F., Reynolds, J.M., Richardson, S.J., and Clemmens,
18 S.: Sedimentological, geomorphological and dynamic context of debris-mantled glaciers, Mount
19 Everest (Sagarmatha) region, Nepal, *Quaternary Sci Rev*, 27, 2361-2389, 2008.

20 Inoue, J. and Yoshida, M.: Ablation and heat exchange over the Khumbu Glacier, *Seppyo*,
21 41:26-31, 1980.

22 Kalnay, E., Kanamitsu, M., Kistler, R. et al.: The NCEP/NCAR 40-year reanalysis project,
23 *Bulletin of the American Meteorological Society*, 77, 437-470, 1996.

24 Kayastha, R.B., Takeuchi, Y., Nakawo, M. and Ageta, Y.: Practical prediction of ice melting
25 beneath various thickness of debris cover on Khumbu Glacier, Nepal, using a positive degree-
26 day factor, *Int. Assoc. Hydrol. Sci. Publ.*, 264, 71–81, 2000.

- 1 Lejeune, Y., Bertrand, J., Wagnon, P., and Morin, S.: A physically based model of the year-
2 round surface energy and mass balance of debris-covered glaciers, *J. Glaciol.*, 49(214): 327-344,
3 doi:10.3189/2013JoG12J149, 2013.
- 4 Lettau, H.: Note on aerodynamic roughness-parameter estimation on the basis of roughness-
5 element description, *J. Appl. Meteorol.*, 8:828-832, 1969.
- 6 Munro, D.S.: Surface roughness and bulk heat transfer on a glacier: comparison with eddy
7 correlation, *J. Glaciol.*, 35(121):343-348, 1989.
- 8 Nakawo, M. and Young, G.J.: Field experiments to determine the effect of a debris layer on
9 ablation of glacier ice, *Ann. Glaciol.*, 2:85-91, 1981.
- 10 Nicholson, L. and Benn, D.I.: Calculating ice melt beneath a debris layer using meteorological
11 data, *J. Glaciol.*, 52:463–470, 2006.
- 12 Nicholson, L. and Benn, D.I.: Properties of natural supraglacial debris in relation to modelling
13 sub-debris ice ablation, *Earth Surface Processes and Landforms*, 38(5):490-501,
14 doi:10.1002/esp.3299, 2012.
- 15 Nield, J.M., Chiverrell, R.C., Darby, S.E., Leyland, J., Vircavs, L.H., and Jacobs, B.: Complex
16 spatial feedbacks of tephra redistribution, ice melt and surface roughness modulate ablation on
17 tephra covered glaciers, *Earth Surf. Process. Landforms*, 38, 95-102, doi:10.1002/esp.3352,
18 2013a.
- 19 Nield, J.M., King, J., Wiggs, G.F.S., Leyland, J., Bryant, R.G., Chiverrell, R.C., Darby, S.E.,
20 Eckardt, F.D., Thomas, D.S.G., Vircavs, L.H., and Washington, R.: Estimating aerodynamic
21 roughness over complex surface terrain, *Journal of Geophysical Research: Atmospheres*, 118, 12,
22 948-12, 961, doi:10.1002/2013JD020632, 2013b.
- 23 Østrem, G.: Ice Melting under a thin layer of moraine, and the existence of ice cores in moraine
24 ridges, *Geografiska Annaler*, 41(4):228-230, 1959.
- 25 Rahimi, C.J. and Konrad, J-M.: Thermal conductivity of compacted snow. *Cold Regions*
26 *Engineering: Sustainable Infrastructure Development in a Changing Cold Climate*, ASCE, 833-
27 843, 2012.

1 Rees, W.G. and Arnold, N.S.: Scale-dependent roughness of a glacier surface: implications for
2 radar backscatter and aerodynamic roughness modelling, *J. Glaciol.*, 52(177):214-222, 2006.

3 Reid, T.D. and Brock, B.W.: An energy-balance model for debris-covered glaciers including heat
4 conduction through the debris layer, *J. Glaciol.*, 56(199):903-916, 2010.

5 Reid, T.D., Carenzo, M., Pellicciotti, F. and Brock, B.W.: Including debris cover effects in a
6 distributed model of glacier ablation, *J. Geophys. Res.*, 117(D18), D18105,
7 doi:10.1029/2012JD017795, 2012.

8 Robertson, E.C.: *Thermal Properties of Rocks*. US Geological Survey (No. 88-441), 1988.

9 Rounce, D.R., and McKinney, D.C.: Debris thickness of glaciers in the Everest area (Nepal
10 Himalaya) derived from satellite imagery using a nonlinear energy balance model, *The*
11 *Cryosphere*, 8:1317-1329, doi:10.5194/tc-8-1317-2014, 2014.

12 Smith, M.W.: *Roughness in the Earth Sciences*, *Earth-Science Reviews*, 136, 202-225, 2014.

13 Snavely N.: *Scene reconstruction and visualization from internet photo collections*, Unpublished
14 PhD thesis, University of Washington, USA, 2008.

15 Snavely, N., Seitz, S.M., and Szeliski, R.: Modeling the world from internet photo collections,
16 *Int. J. Comput. Vis.*, 80:189-210, doi:10.1007/s11263-007-0107-3, 2008.

17 Sturm, M., Holmgren, J., König, M., and Morris, K.: The thermal conductivity of seasonal snow,
18 *J. Glaciol.*, 43, 26-41, 1997.

19 Sturm, M., Perovich, D.K., and Holmgren, J.: Thermal conductivity and heat transfer through the
20 snow on the ice of the Beaufort Sea, *J. Geophys. Res.*, 107(C21), 2002.

21 Szeliski, R.: *Computer Vision: algorithms and applications*. Springer, London, 2011.

22 Takeuchi, Y., Kayastha, R. B. and Nakawo, M.: Characteristics of ablation and heat balance in
23 debris-free and debris-covered areas on Khumbu Glacier, Nepal Himalayas, in the pre-monsoon
24 season, *Int. Assoc. Hydrol. Sci. Publ.*, 264, 53–61, 2000.

25 Westoby, M.J., Brasington, J., Glasser, N.F., Hambrey, M.J., and Reynolds, J.M.: ‘Structure-
26 from-Motion’ Photogrammetry: A low-cost, effective tool for geoscience applications,
27 *Geomorphology*, 179:300-314, 2012.

- 1 Zhang, Y., Fujita, K., Liu, S., Liu, Q., and Nuimura, T.: Distribution of debris thickness and its
- 2 effect on ice melt at Hailuogou Glacier, Southeastern Tibetan Plateau, using in situ surveys and
- 3 ASTER imagery, *J. Glaciol.*, 57(206):1147-1157, 2011.

- 1 Table 1. Details of the debris thickness, topography, and monitoring equipment installed at each
 2 site. *Italics* note an estimation of debris thickness. T_s denotes surface temperature.

Site	Debris Thickness (m)	Slope (°)	Aspect (°)	Temperature Sensor Depth (m)	Ablation Stake	z_0 photos
4	<i>1.50</i>	17	232	T_s , 0.10, 0.20, 0.40, 0.83	-	-
5	0.54	24	158	T_s	x	-
6	0.08	37	237	T_s	x	-
7	0.52	31	65	-	x	-
8	0.20	32	187	-	x	-
10	0.07	32	337	-	x	-
11	0.45	32	197	T_s , 0.05, 0.10, 0.20, 0.36	x	-
12	0.15	19	265	-	x	-
13	0.33	29	295	T_s , 0.05, 0.10, 0.20	x	-
14	0.26	23	148	T_s , 0.05, 0.24	x	-
15	0.37	29	40	T_s	x	-
16	0.15	32	264	-	x	-
17	0.27	29	228	T_s	x	-
19	0.37	33	198	T_s	x	-
20	0.20	29	200	T_s	x	-
A	-	-	-	-	-	x
B	-	-	-	-	-	x
C	-	-	-	-	-	x
D	-	-	-	-	-	x

3

1 Table 2. Errors associated with the DEM for each site

Site	DEM Error (m)			Total
	<i>x</i>	<i>y</i>	<i>z</i>	
A	0.015	0.018	0.007	0.024
B	0.004	0.007	0.001	0.008
C	0.010	0.007	0.002	0.012
D	0.006	0.007	0.001	0.009

2

1 Table 3. Surface roughness (z_0) estimates and obstacle thresholds as a function of DEM
 2 resolution (m) at Sites A-D.

Site	DEM	Obstacle	z_0 (m)	
	Resolution (m)	Threshold (m)	avg	std
A	0.01	0.048	0.016	0.008
	0.02	0.052	0.016	0.007
	0.04	0.054	0.015	0.007
B	0.01	0.067	0.043	0.037
	0.02	0.073	0.040	0.029
	0.04	0.078	0.036	0.022
C	0.01	0.024	0.006	0.005
	0.02	0.026	0.006	0.004
	0.04	0.027	0.006	0.006
D	0.01	0.033	0.014	0.012
	0.02	0.037	0.015	0.013
	0.04	0.040	0.014	0.011

3
4

1 Table 4. Optimized values of albedo, thermal conductivity, and surface roughness for three
 2 methods of estimating latent heat flux during calibration period.

Site	LE _{Rain}			LE _{RH100}			LE _{Dry}		
	α	k ¹	z ₀ ²	α	k ¹	z ₀ ²	α	k ¹	z ₀ ²
4	0.26	1.62	0.006	0.24	1.62	0.006	0.23	1.62	0.011
5	0.40	1.62	0.014	0.40	1.62	0.013	0.40	1.62	0.017
6	0.40	1.29	0.043	0.40	1.35	0.043	0.40	1.31	0.043
11	0.37	1.62	0.006	0.37	1.62	0.006	0.39	1.62	0.006
13	0.10	0.92	0.025	0.16	1.03	0.015	0.10	1.62	0.021
14	0.39	1.61	0.015	0.40	1.62	0.012	0.39	1.62	0.017
15	0.38	1.62	0.006	0.37	1.62	0.006	0.38	1.62	0.006
17	0.30	1.62	0.006	0.30	1.55	0.006	0.30	1.62	0.006
19	0.33	1.62	0.019	0.37	1.62	0.013	0.30	1.62	0.028
20	0.28	1.62	0.006	0.29	1.62	0.006	0.30	1.62	0.006
Avg	0.32	1.52	0.015	0.33	1.53	0.013	0.32	1.59	0.016
Std	0.09	0.23	0.012	0.08	0.19	0.011	0.10	0.10	0.012

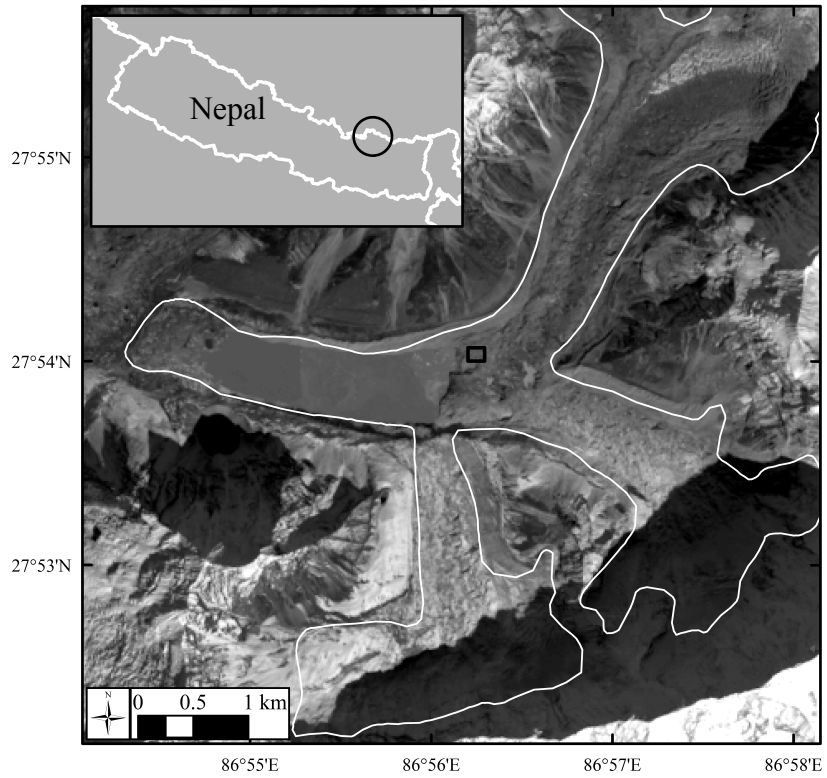
¹units of W m⁻¹ K⁻¹; ²units of m

3

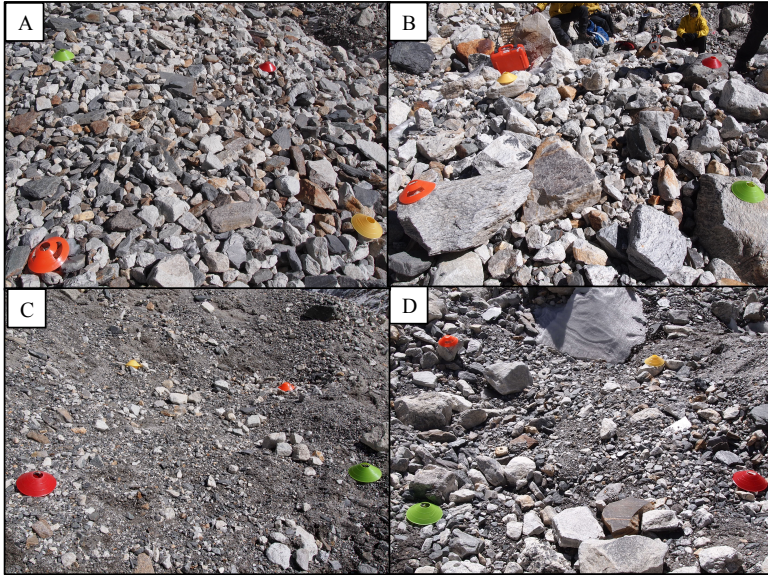
1 Table 5. Sensitivity analysis showing percent changes relative to the total melt (m) as a function
 2 of the uncertainty associated with the calibrated parameters (α , k , z_0) for all sites over the study
 3 period using the LE_{Rain} model in conjunction with the average calibrated parameters for all sites.

Parameter		α		k		z_0	
<i>Adjustment</i>		<i>+ 0.10</i>	<i>- 0.10</i>	<i>+ 0.40</i>	<i>- 0.40</i>	<i>+ 0.010</i>	<i>- 0.010</i>
Site	Total Melt (m)	% Change					
4	0.30	-12.3	+13.0	+30.1	-29.4	-9.7	+21.7
5	0.90	-12.6	+13.0	+22.3	-24.0	-9.2	+19.4
6	2.70	-11.1	+11.3	+13.1	-16.3	-4.1	+7.9
7	0.92	-12.6	+12.6	+22.0	-23.5	-8.8	+18.8
8	1.03	-11.6	+11.9	+20.7	-22.5	-7.7	+16.1
10	1.61	-12.2	+12.1	+18.9	-21.2	-7.7	+15.3
11	1.12	-12.0	+12.5	+20.3	-22.1	-7.7	+16.2
12	1.30	-11.8	+12.0	+19.8	-21.9	-7.8	+16.1
13	1.05	-12.4	+12.7	+21.2	-22.9	-8.5	+17.8
14	1.72	-11.9	+11.8	+18.1	-20.7	-7.0	+14.1
15	0.90	-12.4	+12.9	+21.8	-23.4	-8.6	+17.7
16	1.76	-11.6	+12.1	+18.3	-20.2	-6.7	+14.0
17	2.77	-10.8	+11.1	+12.0	-15.0	-2.9	+5.7
19	2.04	-11.6	+11.7	+16.5	-19.4	-6.3	+12.3
20	1.81	-11.4	+11.4	+16.5	-19.4	-6.1	+12.1
Average		-11.9	+12.1	+19.4	-21.5	-7.3	+15.0

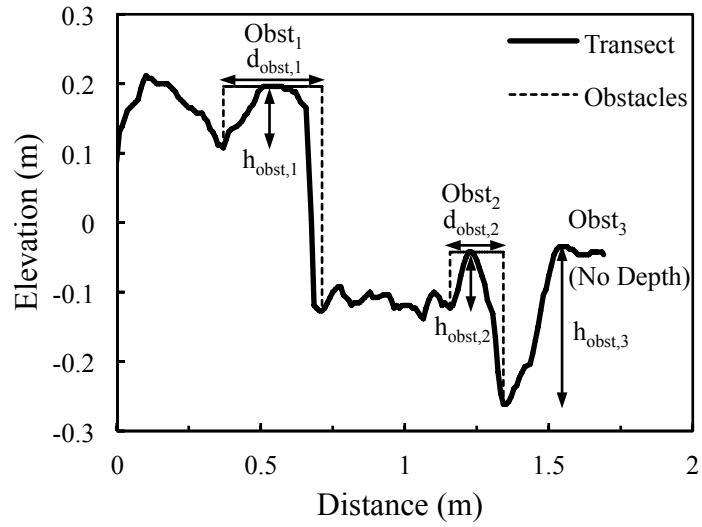
4



1
2 Figure 1. Landsat 8 panchromatic image from 14 Nov 2014 of Imja-Lhotse Shar glacier with the
3 focus area of this study highlighted by the rectangular box several kilometers up-glacier from the
4 terminus, and the site location within Nepal shown in the inset.

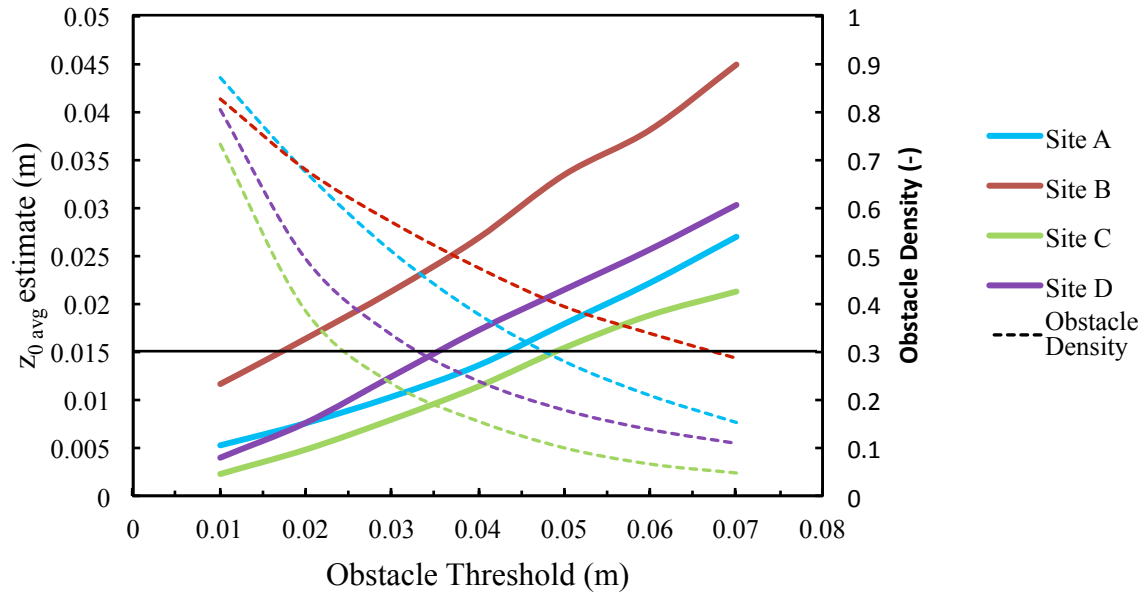


1
2 Figure 2. Sites A-D highlighting the variations in grain sizes that are found over the debris-
3 covered portion of Imja-Lhotse Shar glacier (cones 0.19 m diameter).
4

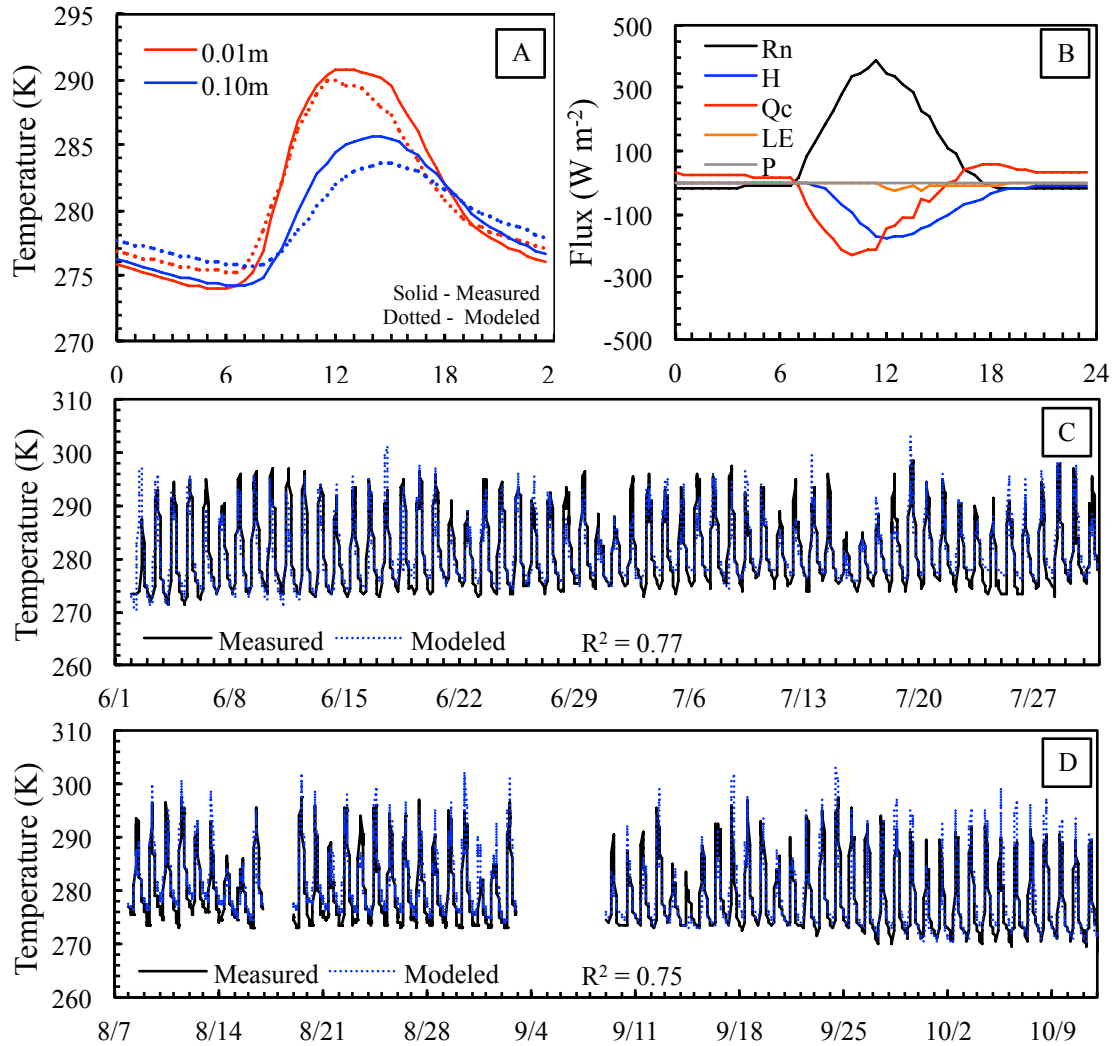


1
2
3
4

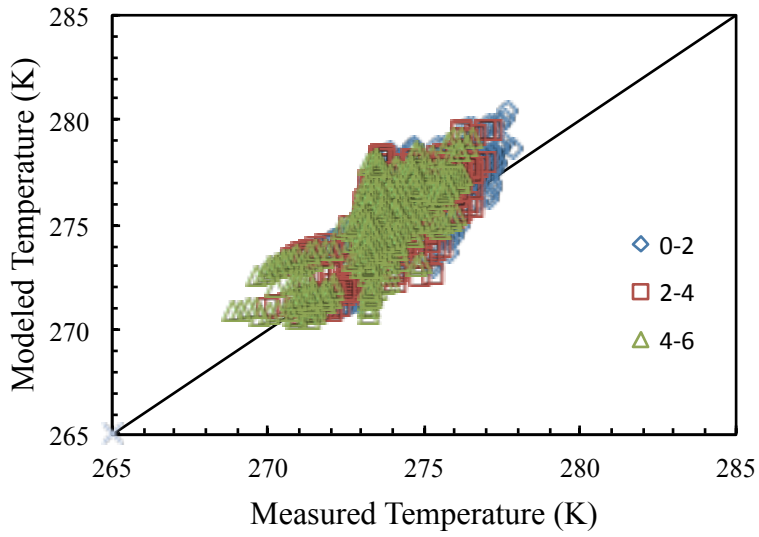
Figure 3. Transect from Left-Right of Site B showing the identification of obstacles (Obst) and their corresponding heights (h_{obst}) and depths (d_{obst}).



1
 2 Figure 4. The effect of obstacle threshold (m) on both obstacle density and the estimate of
 3 surface roughness using the modified method for Sites A-D and the DEMs with a resolution of
 4 0.01 m.

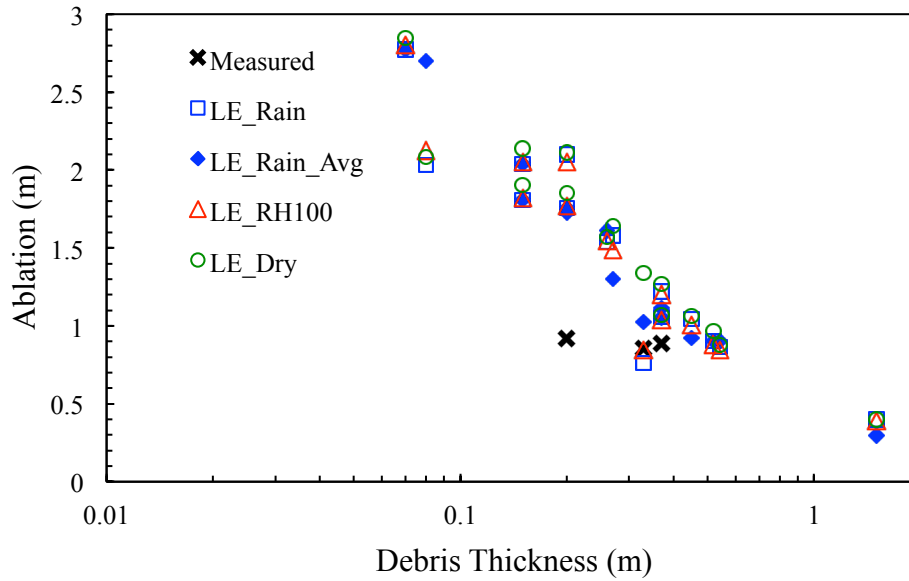


1
 2 Figure 5. Various plots for Site 11 using the LE_{Rain} model showing (A) average daily
 3 temperatures at two depths (solid and dashed lines indicate measured and modeled temperatures,
 4 respectively), (B) average daily energy fluxes, (C) measured and modeled temperatures at a
 5 depth of 0.01 m over the calibration period, and (D) measured and modeled temperatures over
 6 the validation period.

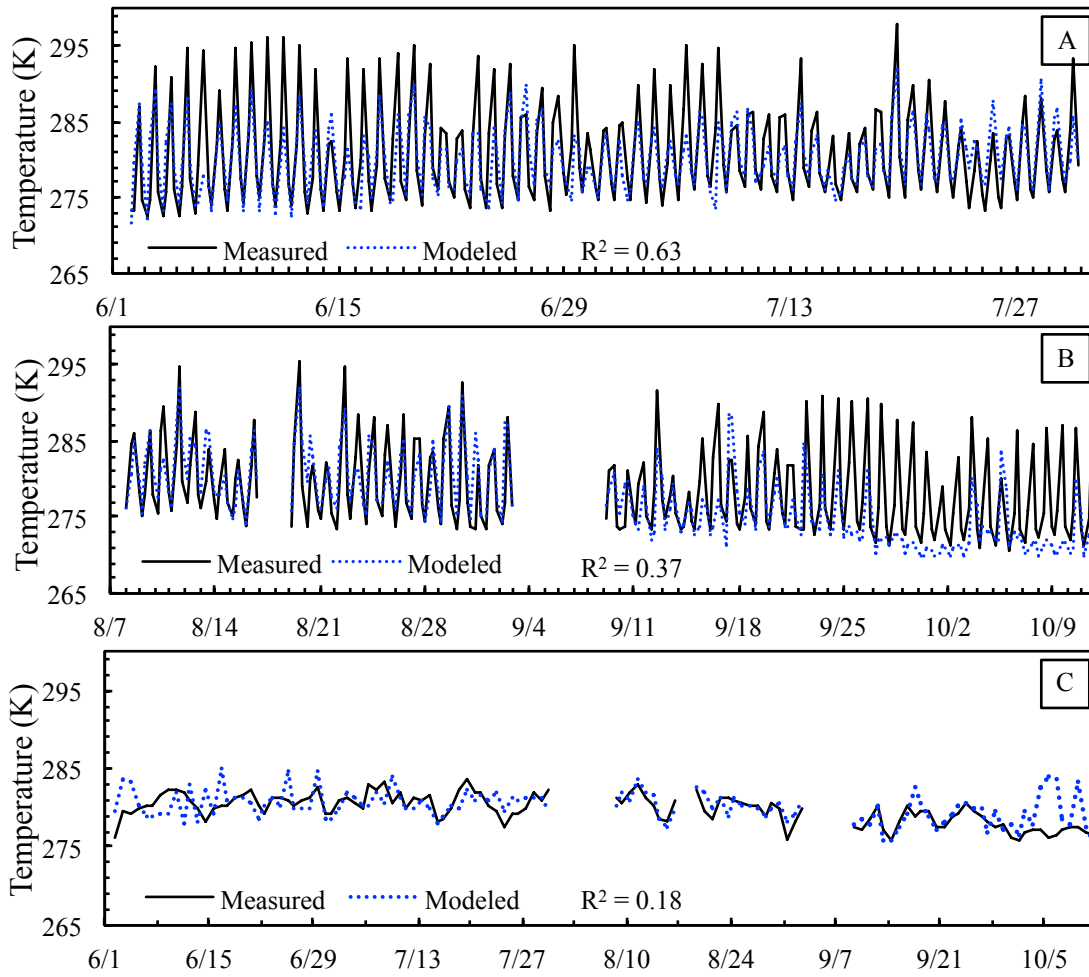


1

2 Figure 6. Scatterplot of measured and modeled temperature for Site 11 at the surface for the
3 LE_{Rain} model showing the positive temperature bias overnight.



1
 2 Figure 7. Modeled ablation with respect to debris thickness for all 15 sites from 18 May to 09
 3 November 2014 for each of the three latent heat flux models including the LE_{Rain} model with
 4 average values and the three measured stakes that did not exceed 1 m.
 5



1
 2 Figure 8. Modeled and measured surface temperature at Site 11 over the (A) calibration period
 3 and (B) validation period using 6-hour data, and (C) entire period using daily averages.